Supporting Information

Material design in converting an oxidative-type $BiVO_4$ catalyst into a reductive $BiV(S,O)_{4-x}$ sulfo-oxide catalyst for nitrogen photoreduction to ammonia

Xiaoyun Chen[1,*], Pengkun Zhang[1], Dong-Hau Kuo[2,*], Qinhan Wu[1], Adugna Boke Abdeta[1], Binhong Wu[1], Zhengjie Su[1], Longyan Chen[1], Osman Ahmed Zelekew[3], Jinguo Lin[1,*]

[1]College of Materials Engineering, Fujian Agriculture and Forestry University, Fuzhou 350002, China

[2]Department of Materials Science and Engineering, National Taiwan University of Science and Technology, Taipei 10607, Taiwan

[3]Department of Materials Science and Engineering, Adama Science and Technology University, Adama, Ethiopia

*Corresponding author

E-mail address: dhkuo@mail.ntust.edu.tw (D.-H. Kuo)

E-mail address: fjlinjg@126.com (J. G. Lin)

E-mail address: fjchenxy@126.com (X. Y. Chen)

Experimental Section

1. Computation of apparent quantum efficiency (AQE) and solar-to-ammonia (STA) conversion efficiency

According to the literature reports [1], the apparent quantum efficiency (AQE) is determined. The catalytic experiments for determining AQE were performed in pure water (100 mL) without any sacrificial reagents. 50 mg of BiVOS-2, used as the photocatalyst, was added to the solution. The reaction solution was irradiated by a 300 W Xe lamp with a band-pass filter for the wavelength of 420 nm. The photon flux of the incident light was measured by a CEL-NP2000 photoradiometer. The AQE is calculated according to the equation below:

$$\mathrm{AQE} = \frac{Number\ of\ reacted\ electrons}{Number\ of\ incident\ photons} \times 100\% = \frac{6 \cdot n_{AM} \cdot N_A}{\frac{W \cdot A \cdot t}{h \cdot v}} \times 100\%$$

where n_{AM} represents the molar number of generated ammonia, while *W*, *A*, *t*, and *v* are for the incident light intensity, irradiation area, time, and frequency, respectively. N_{A} and *h* are Avogadro's constant and Planck constant, respectively.

According to the literature reports [2,3], to determine the Solar-to-Ammonia (STA) conversion efficiency, reactions were performed using a solar simulator, where the efficiency was calculated as:

$$\mathrm{STA} = \frac{[\Delta \mathrm{G\ for}\ NH_3\ \mathrm{generation\ (J \cdot mol^{-1})}] \times [\ NH_3\ \mathrm{evolved\ (mol)}]}{[\mathrm{total\ input\ energy\ (W)}] \times [\mathrm{reaction\ time\ (s)}]} \times 100\%$$

In the above equations, the ΔG° values for NH_3 generation is 339 kJ·mol^{-1}. The overall irradiance of the AM1.5G spectrum was 100 mW cm^{-2} and the irradiation area was 4.26 cm^2 .

2. NH_3 product characterization and qualification.

2.1 Indophenol blue method

Following the literature reports [4,5]: 4 mL solution reaction solution was mixed with 50 μL of catalyst solution (1% BiVOS aqueous solution), 500 μL coloring solution (aqueous solution of 0.4 M $C_7H_5O_3Na$ and 0.32 M NaOH) and 50 μL oxidizing solution [NaClO (ρCl = 4–4.9) solution containing 0.75 M NaOH] in turn. Then, the mixture was allowed to stand at 25 °C for 2h. The standard curve was obtained from the absorbance at 660 nm.

2.2 Ion chromatography test conditions

According to the literature reports [6]: The Thermo Fisher ICS-600 cationic ion chromatograph with Pac CS12 A 4×250 mm (ICS), was further used to determine the NH_3 concentration. The testing conditions as listed in the table S1.

Table S1 ICS determine the conditions of the NH_3 concentration

Conditions	**Details**	**Conditions**	**Details**
Analytical column	Ion Pac CS12 A 4×250 mm	Run time	15 min
Protective column	Ion Pac CG12A 4×50 mm	Detector	Conductivity detector
Leacheate	20 mM Methyl sulfonic acid aqueous solution	Suppressor	CDRS 600 (4 mm) Self-circulation inhibition
Flow rate	1.0 mL/min	Sample injector	AS-DV
Sample volume	10 ul	Sampling mode	Automatic sampling

3. Density functional theory calculation

The density functional theory (DFT) calculation was performed with the Vienna ab initio simulation package (VASP) by using the projector augmented wave (PAW) function method [7]. A plane-wave basis set was adopted to expand the smooth part of wave functions. The generalized gradient approximation (GGA) with Perdew–Burke-Ernzerhof (PBE) function was used for considering the electron exchange and correlation effect [8, 9]. A 2×2×2 supercell with 52 atoms was adopted for structures considered in this study. Dispersion correction (DFT-D3) proposed by Grimme was employed to describe the Van-Der-Waals force accurately. In the process of geometry optimization, atomic relaxation was considered by referring to the Hellmann-Feynman force smaller than 0.02 eV/Å. The convergence criterion was set to have low energy of 1×10^{-5} eV during the electronic self-consistent loop. The Brillouin-zone integration used the gamma-centered (2×2×1) k-point grids for the geometry optimization [10]. Bader charge population analysis was used to compute the atomic charge [11,12]. The adsorption energy ($E_{ads.}$) of adsorbates is calculated from the equation:

$$E_{ads.} = E_{tot.} - E_{cat.} - E_{N2}$$

where the $E_{tot.}$, $E_{cat.}$, and E_{N2} represent the total energy of the complex of the catalysts and N_2, the energy of the catalysts, and the energy of the isolated N_2 molecule, respectively.

Additional figures and tables

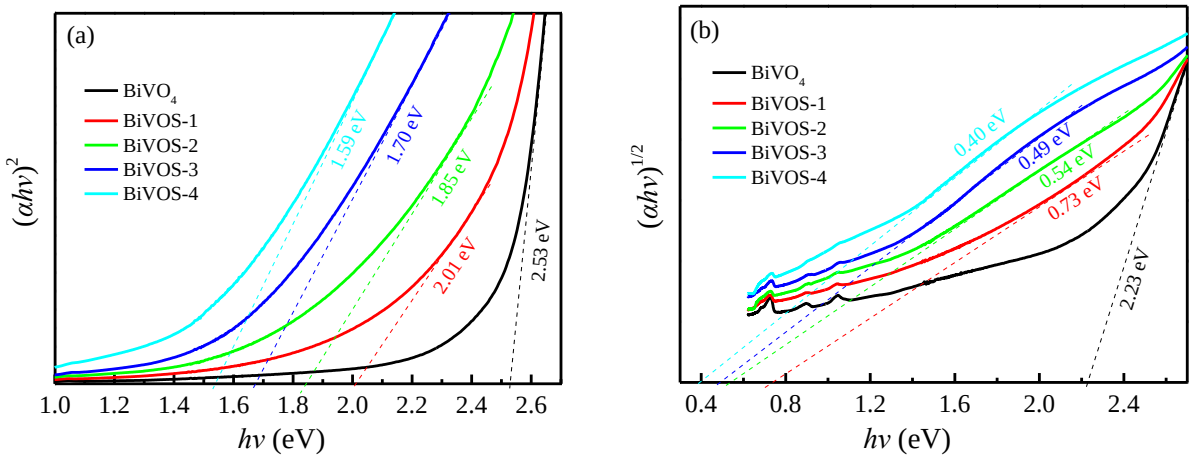

Fig. S1 The ultraviolet-visible absorption spectra of $BiVO_4$, and BiVOS catalysts converted to (a) the $(\alpha hv)^2$ - hv plots for the direct bandgap calculation and (b) the $(\alpha hv)^{1/2}$ - hv plots for the indirect bandgap calculation.

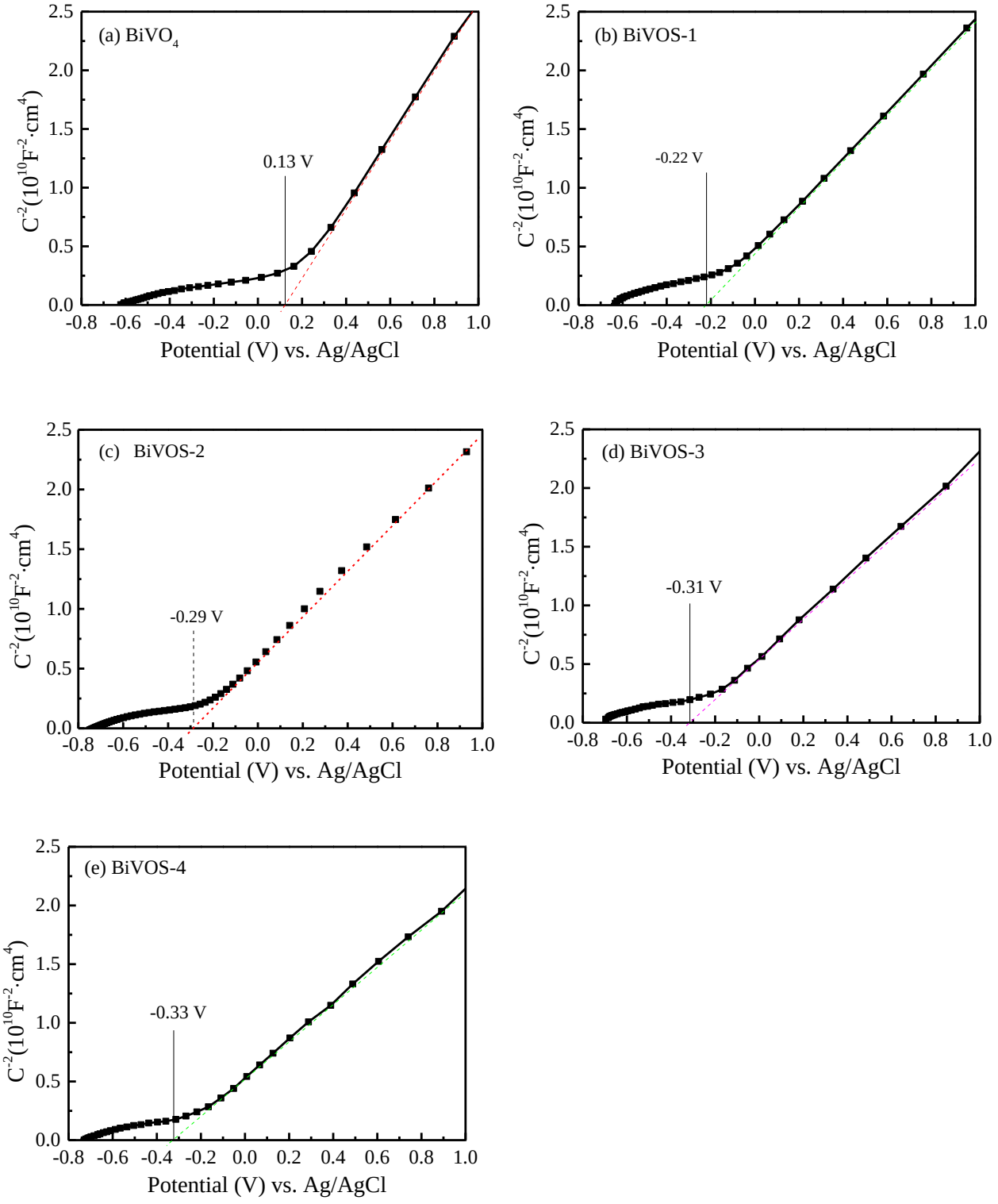

Fig. S2 (a-d) Mott–Schottky curves of $BiVO_4$ and BiVOS catalysts conducting at 1000 Hz.

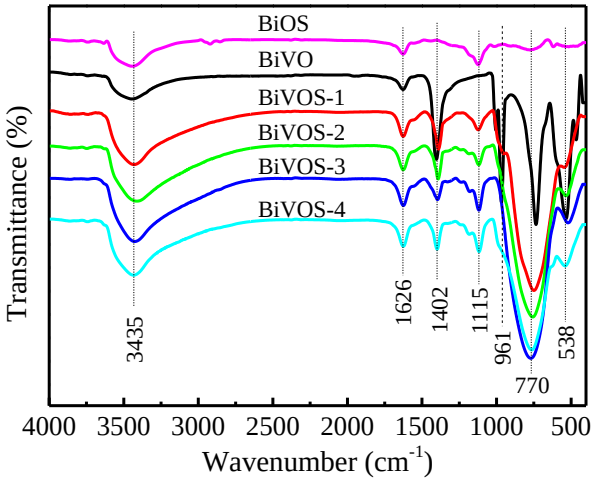

Fig. S3 FTIR spectra of BiOS, $BiVO_4$, and BiVOS catalysts.

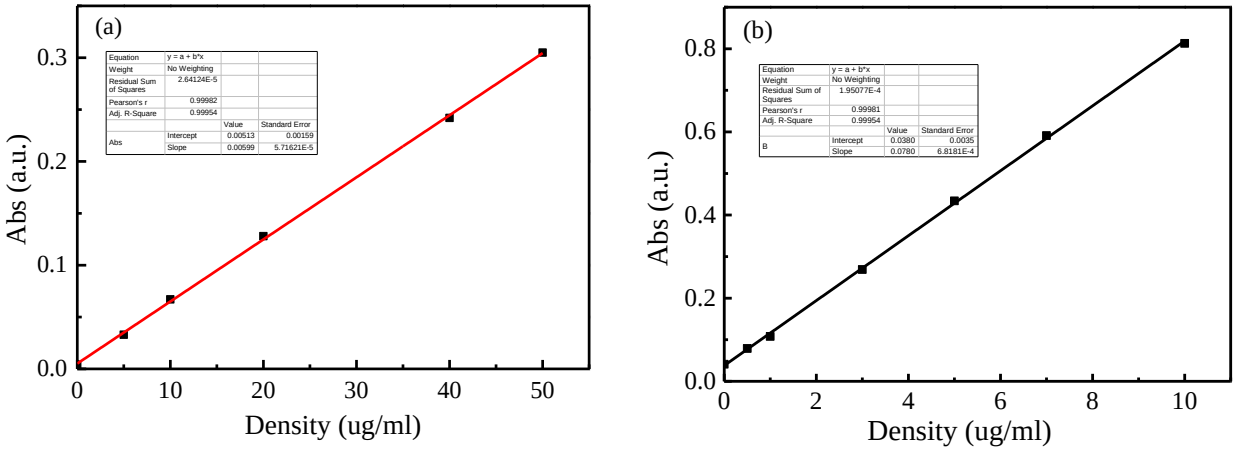

(c)

Injection Name	Ret.Time min ECD_1	Area µS*min ECD_1	Height µS ECD_1	Amount ECD_1
	NH4+	NH4+	NH4+	NH4+
0.5	4.757	0.0615	0.409	0.273
1	4.764	0.1184	0.772	0.920
2	4.767	0.2203	1.402	2.104
5	4.781	0.4793	2.851	5.279
10	4.774	0.8392	4.753	10.197
20	4.787	1.3800	7.448	19.439
30	4.787	1.7911	9.359	30.373
40	4.797	2.1545	11.008	n.a.
50	4.807	2.5703	12.926	n.a.
Average	4.780			
Rel. Std. Dev.	0.341 %			

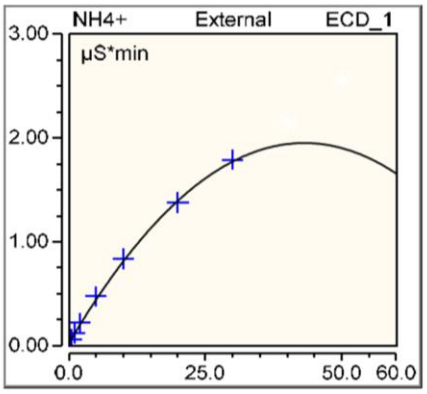

Fig. S4 The standard curve of (a) Nessler's reagent, (b) indophenol bule, and (c) ion chromatography for ammonium ion concentration detection.

Table S2 XPS composition and physical characteristics of $BiVO_4$ and BiVOS catalysts

Catalyst	Molar percentage /%				O molar percentage /%		$V^{4+}/(V^{4+}+V^{5+})$ (%)	Anion/ Cation	S_{BET} (m^2/g)	Crystal size /nm
	Bi	V	S	O	$O_{Lattice}$	V_O				
$BiVO_4$	16.65	16.69	—	66.66	100	—	—	2.00	26.8	13.5
BiVOS-1	17.42	17.35	4.36	60.87	93.17	6.83	3.45	1.88	31.2	11.8
BiVOS-2	17.76	17.70	7.08	57.46	77.49	22.51	17.86	1.82	31.9	11.3
BiVOS-3	18.24	18.18	8.46	55.12	82.74	17.26	11.62	1.75	32.5	11.1
BiVOS-4	18.56	18.49	9.58	53.47	91.68	8.32	5.35	1.70	32.7	10.8
BiVOS-2 after reaction	17.77	17.66	7.12	57.45	77.55	22.45	17.91	1.82	—	11.4

Table S3 Element contents from SEM-EDS analyses for $BiVO_4$ and BiVOS catalysts

Catalyst	Bi	V	S	O	Bi/V
$BiVO_4$	16.47	16.39	—	67.14	0.993
BiCeOS-1	17.34	17.53	4.18	60.95	0.993
BiCeOS-2	17.60	17.76	6.99	57.65	0.992
BiCeOS-3	18.03	18.26	8.34	55.37	0.992
BiCeOS-4	18.33	18.64	9.25	53.78	0.994

Table S4 Element contents from XRF analyses for $BiVO_4$ and BiVOS catalysts

Catalysts	Bi	V	S	O	Bi/Ce
$BiVO_4$	16.61	16.69	—	66.70	0.995
BiCeOS-1	17.61	17.59	4.23	60.57	0.992
BiCeOS-2	17.83	17.79	7.01	57.37	0.994
BiCeOS-3	18.16	18.11	8.40	55.33	0.994
BiCeOS-4	18.50	18.48	9.39	53.63	0.993

Table S5 The average charge carrier lifetime of $BiVO_4$ and BiVOS catalysts

Catalysts	A_1	τ_1 (ns)	A_2	τ_2 (ns)	R^2	τ_{avg} (ns)
$BiVO_4$	73737.926	1.023	692.698	3.729	0.991	1.113
BiVOS-1	1991.507	4.982	140955.125	1.525	0.996	1.678
BiVOS-2	78690.627	2.575	8817.568	5.797	0.999	3.224
BiVOS-3	8457.489	4.213	377682.855	2.386	0.998	2.455
BiVOS-4	659945.746	1.784	6592.964	4.162	0.997	1.838

Table S6 the testing results via Nessler's reagent, indophenol blue and ion chromatography method

Catalysts	Nessler's reagent ($\mu mol \cdot g^{-1} \cdot h^{-1}$)	indophenol blue ($\mu mol \cdot g^{-1} \cdot h^{-1}$)	ion chromatography ($\mu mol \cdot g^{-1} \cdot h^{-1}$)
BiVOS-1	120.2	124.9	112.5
BiVOS-2	563.6	541.0	519.5
BiVOS-3	406.1	385.7	378.4
BiVOS-4	98.9	92.2	87.6

Table S7 Adsorption energy (E_a, eV) and bond length (L_b, Å) of N_2 on perfect-$BiVO_4$, Vo-$BiVO_4$, perfect-BiVOS, and Vo-BiVOS (0 0 2) surface. Electron transfer (E_t) of N_2 molecule. '+' represents that the electrons are transferred to the catalyst atom.

Catalyst	Adsorption energy/ eV	N≡N bond length /Å	Electron transfer
N_2 molecule	—	1.102	—
Perfect-$BiVO_4$	-0.08	1.113	+0.01
Vo-$BiVO_4$	-0.10	1.117	+0.06
Perfect-BiVOS	-0.15	1.120	+0.04
Vo-BiVOS	-0.52	1.148	+0.22

Table S8 The literature-reported catalysts for photocatalytic N_2 fixation

No.	Catalysts	Light source	Reaction medium	Sacrificial agent	NH_3 evolved $\mu mol \cdot g^{-1} \cdot h^{-1}$	NH_3 analysis methods	AQE/QY and STA conversion efficiency	Ref. (Year)
1	CeO_2-$BiFeO_3$	UV−vis	Water	none	117.77 $\mu mol \cdot g^{-1} \cdot h^{-1}$	Nessler's reagent method	—	[13] (2020)
2	TiO_2/$SrTiO_3$/g-C_3N_4	simulated solar light	Water, ethanol (10%, v/v)	ethanol	2192.0 $\mu mol \cdot g^{-1} \cdot h^{-1}$	Nessler's reagent method	—	[14] (2020)
3	Ag-$KNbO_3$	simulated solar light	Water, ethanol (10%, v/v)	ethanol	385.0 $\mu mol \cdot g^{-1} \cdot h^{-1}$	Nessler's reagent method	—	[15] (2019)
4	$LaCoO_3$:Er^{3+}/ATP	visible	Water, ethanol (10%, v/v)	ethanol	71.5 $\mu mol \cdot g^{-1} \cdot h^{-1}$	Nessler's reagent method	—	[16] (2019)
5	Bi-Bi_2WO_6	simulated solar light	Water	none	86.0 $\mu mol \cdot g^{-1} \cdot h^{-1}$	Nessler's reagent method	—	[17] (2019)
6	c-PAN-Bi_2WO_6	simulated solar light	Water	none	160.0 $\mu mol \cdot g^{-1} \cdot h^{-1}$	Nessler's reagent method	—	[18] (2018)
7	Mo-Bi_5O_7Br	300 W Xe lamp (λ> 420 nm)	Water	none	122.9 $\mu mol \cdot g^{-1} \cdot h^{-1}$	Nessler's reagent method	—	[19] (2021)
8	Fe-BiOBr	300 W Xe lamp (λ> 420 nm)	Water	none	46.1 $\mu mol \cdot g^{-1} \cdot h^{-1}$	Nessler's reagent method	—	[20] (2021)
9	$SrTiO_3$	300 W Xe lamp	Water	none	206.0 $\mu mol \cdot g^{-1} \cdot h^{-1}$	Ion chromatography	AQE= 0.38% at 420 nm	[21] (2021)
10	Mo-doped $W_{18}O_{49}$	300 W Xe lamp (λ> 420 nm)	Na_2SO_3 aqueous solution	Na_2SO_3	195.50 $\mu mol \cdot g^{-1} \cdot h^{-1}$	Nessler's reagent method	AQE= 0.33% at 400 nm	[22] (2018)
11	Au/TiO_2	300 W Xe lamp (λ> 420 nm)	Water, methanol (10%, v/v)	methanol	78.60 $\mu mol \cdot g^{-1} \cdot h^{-1}$	Indophenol-blue method	AQE= 0.82% at 550 nm	[23] (2018)
12	Hydrogenated Bi_2MoO_6	300 W Xe lamp	Water and air	none	1.30 $mmol \cdot g^{-1} \cdot h^{-1}$	Nessler's reagent method	AQE= 2.42% at 420 nm	[24] (2016)
13	$Zn_3In_2S_6$	300 W Xe lamp (λ> 420 nm)	Methanol	methanol	355.20 $mg \cdot L^{-1} \cdot g^{-1}$	Nessler's reagent method	—	[25] (2020)
14	Br-doped BiOCl	300 W Xe lamp (λ> 420 nm)	Water	none	6.30 $\mu mol \cdot h^{-1}$	Nessler's reagent method	—	[26] (2019)
15	MoS_2	500 W Xe lamp	Water	none	325.0 $\mu mol \cdot g^{-1} \cdot h^{-1}$	Indophenol-blue method and ^1H-NMR with $^{15}N_2$ isotope labeling	—	[27] (2017)
16	Cu-doped TiO_2	300 W Xe lamp	Water	none	78.90 $\mu mol \cdot g^{-1} \cdot h^{-1}$	Nessler's reagent method and ion chromatography	AQE= 0.74% at 380 nm = 0.23% at 420 nm	[28] (2019)

17	Fe-doped BiOCl	300 W Xe lamp	Water	none	1.02 mmol·g^{-1}·h^{-1}	Indophenol-blue method and ^{1}H-NMR with $^{15}N_2$ isotope labeling	AQE= 1.80% at 420 nm	[29] (2019)
18	Fe-doped BiOBr	300 W Xe lamp (λ> 420 nm)	Water	none	382.68 μmol·g^{-1}·h^{-1}	Nessler's reagent method, ^{1}H NMR, mass spectroscopy with $^{15}N_2$ isotope labeling	—	[30] (2020)
19	Bi_2MoO_6/BiOBr	300 W Xe lamp visible light	Water	none	90.70 μmol·g^{-1}·h^{-1}	Nessler's reagent method	—	[31] (2019)
20	P-doped g-C_3N_4	2 KW Xe lamp (λ> 420 nm)	Water	none	0.20 μmol·h^{-1}	Ion chromatography	STA= 0.1%	[2] (2018)
21	S-doped g-C_3N_4	500 W Xe lamp	Water, methanol (4%, v/v)	methanol	5.99 mmol·g^{-1}·h^{-1}	Nessler's reagent method	—	[32] (2018)
22	Defected Bi_3O_4Br nanosheets	300 W Xe lamp	Water	none	380.0 μmol·g^{-1}·h^{-1}	Nessler's reagent method and ion chromatography	AQE= 1.59% at 400 nm	[33] (2019)
23	Bi_5O_7Br nanotubes	300 W Xe lamp (λ> 420 nm)	Water	none	1.38 mmol·g^{-1}·h^{-1}	Nessler's reagent method	AQE= 2.3% at 420 nm	[34] (2017)
24	Yb^{3+}/Tm^{3+} co-doped CeF_3	300 W Xe lamp	Water	none	15.06 μmol·g^{-1}·h^{-1}	Nessler's reagent method	—	[35] (2022)
25	WO_3/CdS	300 W Xe lamp	Water	none	35.8 μmol·g^{-1}·h^{-1}	ion chromatography	—	[36] (2022)
26	Cu_2O/SnS_2/SnO_2	300 W Xe lamp	Water, ethanol (20%, v/v)	ethanol	66.35 μmol·g^{-1}·h^{-1}	Nessler's reagent method	—	[37] (2021)
27	La/MoO_{3-x}	300 W Xe lamp	Water	none	209 μmol·g^{-1}·h^{-1}	ion chromatography	—	[38] (2022)
28	AgPt–TiO_2	300 W Xe lamp	Water	none	38.4 μmol·g^{-1}·h^{-1}	ion chromatography	—	[39] (2021)
29	Pt/N–MoS_2	300 W Xe lamp	Water, methanol (10%, v/v)	methanol	133.8 μmol·g^{-1}·h^{-1}	Nessler's reagent method	—	[40] (2020)
30	Ag/B-doped g-C_3N_4	300 W Xe lamp	Water, methanol (5%, v/v)	methanol	305 μmol·g^{-1}·h^{-1}	Nessler's reagent method	—	[41] (2020)
31	UiO-66	300 W Xe lamp	Water, methanol (5%, v/v)	methanol	256 μmol·g^{-1}·h^{-1}	Nessler's reagent method	—	[42] (2021)
32	Pt/Bi-$KTa_{0.5}Nb_{0.5}O_3$	300 W Xe lamp	Water, methanol (5%, v/v)	methanol	38.57 μmol·g^{-1}·h^{-1}	Nessler's reagent method	—	[43] (2022)

33	$Au/(BiO)_2CO_3$	300 W Xe lamp	Water	none	38.2 $\mu mol \cdot g^{-1} \cdot h^{-1}$	ion chromatography	—	[44] (2017)
34	$Ag/AgBr\text{-}\delta\text{-}Bi_2O_3$	400 W Xe lamp	Water	none	364.2 $\mu mol \cdot g^{-1} \cdot h^{-1}$	Nessler's reagent method	—	[45] (2019)
35	BiO QDs-g-C_3N_4	300 W Xe lamp	Na_2SO_3 (1 mM)	Na_2SO_3	576.11 $\mu mol \cdot g^{-1} \cdot h^{-1}$	Nessler's reagent method	AQE= 0.53% at 420 nm	[46] (2021)
36	g-C_3N_4/Bi_2MoO_6	500 W Xe lamp (λ> 420 nm)	ethanol (17.1 mM)	ethanol	43.61 $\mu mol \cdot g^{-1} \cdot h^{-1}$	Nessler's reagent method	—	[47] (2020)
37	BiVOS	300 W Xe lamp (λ> 420 nm)	Water	none	563.6 $\mu mol \cdot g^{-1} \cdot h^{-1}$	Nessler's reagent method and ion chromatography	AQE= 2.18% at 420 nm STA= 0.071% at AM1.5G	This work

References:

[1] X. Chen, X. Zhang, Y. Li, M. Qi, J. Li, Z. Tang, Z. Zhou, Y. Xu, Transition metal doping BiOBr nanosheets with oxygen vacancy and exposed {102} facets for visible light nitrogen fixation, *Appl. Catal. B-Environ.*, 281 (2021) 119516

[2] Y. Shiraishi, S. Shiota, Y. Kofuji, M. Hashimoto, K. Chishiro, H. Hirakawa, S. Tanaka, S. Ichikawa, T. Hirai, Nitrogen fixation with water on carbon-nitride-based metal-free photocatalysts with 0.1% Solar-to-Ammonia energy conversion efficiency. *ACS Appl. Energy Mater*., 1 (2018) 4169–4177.

[3] Z. Chen, T.F. Jaramillo, T.G. Deutsch, A. Kleiman-Shwarsctein, A.J. Forman, N. Gaillard, R. Garland, K. Takanabe, C. Heske, M. Sunkara, E.W. McFarland, K. Domen, E.L. Miller, J.A. Turner, H.N. Dinh, Accelerating materials development for photoelectrochemical hydrogen production: Standards for methods, definitions, and reporting protocols, *J. Mater. Res.*, 25 (2010) 3-16.

[4] T. Hu, G. Jiang, Y. Yan, S. Lan, J. Xie, Q. Zhang, Y. Li, Facile synthesis of Fe single-atom porous photocatalysts via direct metal atomization achieving efficient photocatalytic nitrogen fixation, *J. Mater. Sci. Technol.*, 167 (2023) 248–257

[5] Y. Zhao, F. Wu, Y. Miao, C. Zhou, N. Xu, R. Shi, L.-Z. Wu, J. Tang, T. Zhang, Revealing ammonia quantification minefield in photo/electrocatalysis, *Angew. Chem. Int. Ed.* 10.1002/anie.202108769.

[6] N. Zhang, A. Jalil, D. Wu, S. Chen, Y. Liu, C. Gao, W. Ye, Z. Qi, H. Ju, C. Wang, X. Wu, L. Song, J. Zhu, Y. Xiong, Refining defect states in $W_{18}O_{49}$ by Mo doping: A strategy for tuning N_2 activation towards solar-driven nitrogen fixation, *J. Am. Chem. Soc.*, 140 (2018) 9434-9443.

[7] J.F. G. Kressea, Efficiency of ab-initio total energy calculations for metals and semiconductors using a plane-wave basis set, *Comp. Mater. Sci.*, 6 (1996) 15–50.

[8] K.B. J.P. Perdew, M. Ernzerhof, Generalized gradient approximation made simple, *Phys. Rev. Lett.*, 77 (1996) 3865.

[9] F.A.A.I.L. V. Anisimov, First-principles calculations of the electronic structure and spectra of strongly correlated systems the LDA+ U method, *J. Phys-Condens. Mat.*, 9 (1997) 767.

[10] V.V. Anisimov, J. Zaanen, O.K. Andersen, Band theory and Mott insulators: Hubbard U instead of Stoner I, *Physical review. B, Condensed Matter.*, 44 (1991) 943–954.

[11] E. Sanville, S.D. Kenny, R. Smith, G. Henkelman, Improved grid-based algorithm for bader charge allocation, *J. Comput. Chem.*, 28 (2007) 899–908.

[12] G. Henkelman, A. Arnaldsson, H. Jónsson, A fast and robust algorithm for bader decomposition of charge density, *Comp. Mater. Sci.*, 36 (2006) 354–360.

[13] Mansingh, S.; Sultana, S.; Acharya, R.; Ghosh, M.; Parida, K.Efficient photon conversion via double charge dynamics CeO_2−$BiFeO_3$ p−n heterojunction photocatalyst promising toward N_2 fixation and phenol−Cr (VI) detoxification. *Inorg. Chem.*, 59 (2020) 3856−3873.

[14] R. Tao, X. Li, X. Li, C. Shao, Y. Liu, TiO_2/$SrTiO_3$/g-C_3N_4 Ternary heterojunction nanofibers: Gradient energy band, cascade charge transfer, enhanced photocatalytic hydrogen evolution, and nitrogen fixation. *Nanoscale*, 12 (2020) 8320−8329.

[15] P. Xing, S. Wu, Y. Chen, P. Chen, X. Hu, H. Lin, L.H. Zhao, Y. He, New application and excellent performance of Ag/$KNbO_3$ nanocomposite in photocatalytic NH_3 synthesis. *ACS Sustain. Chem. Eng*., 7 (2019) 12408−12418.

[16] H. Zhang, X. Li, H. Su, X. Chen, S. Zuo, X. Yan, W. Liu, C. Yao, Sol−Gel synthesis of upconversion perovskite/attapulgite heterostructures for photocatalytic fixation of nitrogen. *J. Sol-Gel Sci. Technol*., 92 (2019) 154−162.

[17] S. Zhou, C. Zhang, J. Liu, J. Liao, Y. Kong, Y. Xu, G. Chen, Formation of an priented Bi_2WO_6 photocatalyst induced by in situ bi reduction and its use for efficient nitrogen fixation. *Catal. Sci. Technol*., 9 (2019) 5562−5566.

[18] C. Zhang, G. Chen, C. Lv, Y. Yao, Y. Xu, X. Jin, Q. Meng, Enabling nitrogen fixation on Bi_2WO_6 Photocatalyst by C-PAN Surface Decoration. *ACS Sustain. Chem. Eng*., 2018, 6 (9), 11190**–**11195.

[19] X. Chen, M.Y. Qi, Y.H. Li, Z.R. Tang, Y.J. Xu, Enhanced ambient ammonia photosynthesis by Mo−doped Bi_5O_7Br nanosheets with light−switchable oxygen vacancies, *Chinese J. Catal.,* 42 (2021) 2020–2026.

[20] X. Chen, X. Zhang, Y.H. Li, M.Y. Qi, J.Y. Li, Z.R. Tang, Z. Zhou, Y.J. Xu, Transition metal doping BiOBr nanosheets with oxygen vacancy and exposed {102} facets for visible light nitrogen fixation, *Appl. Catal. B-Environ*., 281 (2021) 119516.

[21] J. Wang, T. Wang, Z. Zhao, R. Wang, C. Wang, F. Zhou, S. Li, L. Zhao, M. Feng, Regulation of oxygen vacancies in $SrTiO_3$ perovskite for efficient photocatalytic nitrogen fixation, *Journal of Alloys and Compounds: An Interdisciplinary Journal of Materials Science and Solid-state Chemistry and Physics*, 902 (2022) 163865**–**163872.

[22] N. Zhang, A. Jalil, D. Wu, S. Chen, Y. Liu, C. Gao, W. Ye, Z. Qi, H. Ju, C. Wang, Refining defect states in $W_{18}O_{49}$ by Mo doping: A strategy for tuning N_2 activation towards solar-driven nitrogen fixation, *J. Am. Chem. Soc.,* 140 (2018) 9434.

[23] J. Yang, Y. Guo, R. Jiang, F. Qin, H. Zhang, W. Lu, J. Wang, J.C. Yu, High-efficiency "working-in-tandem" nitrogen photofixation achieved by assembling plasmonic gold nanocrystals on ultrathin titania nanosheets, *J. Am. Chem. Soc.*, 140 (2018) 8497.

[24] Y. Hao, X. Dong, S. Zhai, H. Ma, X. Wang, X. Zhang, Hydrogenated bismuth molybdate nanoframe for efficient sunlight‐driven nitrogen fixation from air, *Chem. Eur. J.*, 22 (2016) 18722.

[25] H. Han, Y. Yang, J. Liu, X. Zheng, X. Wang, S. Meng, S. Zhang, X. Fu, S. Chen, Effect of Zn vacancies in $Zn_3In_2S_6$ nanosheets on boosting photocatalytic N_2 Fixation, *ACS Appl. Energ. Mater.*, 3 (2020) 11275.

[26] D. Wu, R. Wang, C. Yang, Y. An, H. Lu, H. Wang, K. Cao, Z. Gao, W. Zhang, F. Xu, Br doped porous bismuth oxychloride micro-sheets with rich oxygen vacancies and dominating {001} facets for enhanced nitrogen photo-fixation performances, *J. Colloid Interf. Sci.*, 556 (2019) 111.

[27] S. Sun, X. Li, W. Wang, L. Zhang, X, Sun, Photocatalytic robust solar energy reduction of dinitrogen to ammonia on ultrathin MoS_2, *Appl. Catal. B-Environ*., 200 (2017) 323.

[28] Y. Zhao, Y. Zhao, R. Shi, B. Wang, G.I.N. Waterhouse, L.Z. Wu, C.H. Tung, T. Zhang, Tuning oxygen vacancies in ultrathin TiO_2 nanosheets to boost photocatalytic nitrogen fixation up to 700 nm, *Adv. Mater.*, 31 (2019) 1806482.

[29] N. Zhang, L. Li, Q. Shao, T. Zhu, X. Huang, X. Xiao, Fe-doped BiOCl nanosheets with light-switchable oxygen vacancies for photocatalytic nitrogen fixation, *ACS Appl. Energ. Mater.*, 2 (2019) 8394.

[30] Y. Liu, Z. Hu, J. C. Yu, Fe enhanced visible-light-driven nitrogen fixation on BiOBr nanosheets, *Chem. Mater.*, 32 (2020) 1488–1494.

[31] X. Xue, R. Chen, C. Yan, Y. Hu, W. Zhang, S. Yang, L. Ma, G. Zhu, Z. Jin, Efficient photocatalytic nitrogen fixation under ambient conditions enabled by the heterojunctions of n-type Bi_2MoO_6 and oxygen-vacancy-rich p-type BiOBr, *Nanoscale*, 11 (2019) 10439.

[32] S. Cao, B. Fan, Y. Feng, H. Chen, F. Jiang, X. Wang, Sulfur-doped g-C_3N_4 nanosheets with surface carbon vacancies: General synthesis and improved activity for simulated solar-light photocatalytic nitrogen fixation, *Chem. Eng. J.*, 353 (2018) 147–156.

[33] J. Di, J. Xia, M. F. Chisholm, J. Zhong, C. Chen, X. Cao, F. Dong, Z. Chi, H. Chen, Y. X. Weng, Defect-tailoring mediated electron-hole separation in single-unit-cell Bi_3O_4Br nanosheets for boosting photocatalytic hydrogen evolution and nitrogen fixation, *Adv. Mater.*, 31 (2019) 1807576.

[34] S. Wang, X. Hai, X. Ding, K. Chang, Y. Xiang, X. Meng, Z. Yang, H. Chen, J. Ye, Photocatalysis: Light-switchable oxygen vacancies in ultrafine Bi_5O_7Br nanotubes for boosting solar-driven nitrogen fixation in pure water, *Adv. Mater., 29* (2017) 1701774.

[35] M. Zhong, Z. Wang, D. Dai, B. Yang, S. Zuo, C. Yao, F. Wu, X. Li, Upconversion hollow nanospheres CeF_3 co-doped with Yb^{3+} and Tm^{3+} for photocatalytic nitrogen fixation. *J. Rare Earth.*, 40 (2022) 586–594

[36] P. Xia, X. Pan, S. Jiang, J. Yu, B, He, P.M. Ismail, W. Bai, J. Yang, H. Zhang, M. Cheng, H. Li, Q. Zhang, C. Xiao, Y. Xie, Designing a redox heterojunction for photocatalytic "overall nitrogen fixation" under mild conditions. *Adv, Mater.*, 34 (2022) 2200563.

[37] N. Ojha, A. Bajpai, S. Kumar, Enriched oxygen vacancies of $Cu_2O/SnS_2/SnO_2$ heterostructure for enhanced photocatalytic reduction of CO_2 by water and nitrogen fixation. *J. Colloid Interf. Sci.*, 585 (2021) 764–77.

[38] X. Liu, Y. Luo, C. Ling, Y. Shi, G. Zhan, H. Li, H. Gu, K. Wei, F. Guo, Z. Ai, L. Zhang, Rare

earth La single atoms supported MoO_{3-x} for efficient photocatalytic nitrogen fixation. *Appl. Catal. B-Environ*., 301 (2022) 120766.

[39] X. Bian, Y. Zhao, S. Zhang, D. Li, R. Shi, C. Zhou, L.Z. Wu, T. Zhang, Enhancing the supply of activated hydrogen to promote photocatalytic nitrogen fixation. *ACS Mater. Lett.*, 3 (2021) 1521–1527.

[40] H. Maimaitizi, A. Abulizi, T. Zhang, K. Okitsu, J. Zhu, Facile photo-ultrasonic assisted synthesis of flower-like Pt/N-MoS_2 microsphere as an efficient sonophotocatalyst for nitrogen fixation. *Ultrason. Sonochem.*, 63 (2020) 104956.

[41] X. Yao, W. Zhang, J. Huang, Z. Du, X. Hong, X. Chen, X. Hu, X. Wang, Enhanced photocatalytic nitrogen fixation of Ag/B-doped g-C_3N_4 nanosheets by one-step in-situ decomposition-thermal polymerization method. *Appl, Catal. Gen.*, 601 (2020) 117647.

[42] W. Gao, X. Li, X. Zhang, S. Su, S. Luo, R. Huang, Y. Jing, M. Luo, Photocatalytic nitrogen fixation of metal–organic frameworks (MOFs) excited by ultraviolet light: Insights into the nitrogen fixation mechanism of missing metal cluster or linker defects. *Nanoscale*, 13 (2021) 7801–7809.

[43] X. Li, L. Chen, J. Wang, J. Zhang, C. Zhao, H. Lin, Y. Wu, Y. He, Novel platinum-bismuth alloy loaded $KTa_{0.5}Nb_{0.5}O_3$ composite photocatalyst for effective nitrogen-to-ammonium conversion. *J. Colloid Interf. Sci.*, 618 (2022) 362–74.

[44] C. Xiao, H. Hu, X. Zhang, D.R. MacFarlane, Nanostructured gold/bismutite hybrid heterocatalysts for plasmon-enhanced photosynthesis of ammonia. *ACS Sustain. Chem. Eng.*, 5 (2017) 10858–63.

[45] X. Gao, Y. Shang, L. Liu, K. Gao, Ag plasmon resonance promoted 2D AgBr-δ-Bi_2O_3 nanosheets with enhanced photocatalytic ability. *J. Alloys Compd.*, 2019, 803: 565–75.

[46] C. Liang, H.Y. Niu, H. Guo, Efficient photocatalytic nitrogen fixation to ammonia over bismuth monoxide quantum dots-modified defective ultrathin graphitic carbon nitride. *Chem. Eng. J.*, 406 (2021) 126868.

[47] E. Vesali-Kermani, A. Habibi-Yangjeh, H. Diarmand-Khalilabad, S. Ghosh, Nitrogen photofixation ability of g-C_3N_4 nanosheets/Bi_2MoO_6 heterojunction photocatalyst under visible-light illumination. *J. Colloid Interf. Sci.*, 563 (2020) 81–91.